remote sensing

MDPI

Article

Source Characteristics of the 28 September 2018 Mw 7.4 Palu, Indonesia, Earthquake Derived from the Advanced Land Observation Satellite 2 Data

Yongzhe Wang [1,*], Wanpeng Feng [2,3], Kun Chen [1] and Sergey Samsonov [4]

1 Institute of Geophysics, China Earthquake Administration, Beijing 100081, China
2 Guangdong Provincial Key Laboratory of Geodynamics and Geohazards, School of Earth Sciences and Engineering, Sun Yat-sen University, Guangzhou 510275, China
3 Southern Marine Science and Engineering Guangdong Laboratory, Zhuhai 519082, China
4 Canada Centre for Mapping and Earth Observation, Natural Resources Canada, Ottawa, ON K1A0E4, Canada
* Correspondence: yzwang@cea-igp.ac.cn; Tel.: +86-10-6872-9449

Received: 18 July 2019; Accepted: 21 August 2019; Published: 24 August 2019

Abstract: On 28 September 2018, an Mw 7.4 earthquake, followed by a tsunami, struck central Sulawesi, Indonesia. It resulted in serious damage to central Sulawesi, especially in the Palu area. Two descending paths of the Advanced Land Observation Satellite 2 (ALOS-2) synthetic aperture radar (SAR) data were processed with interferometric synthetic aperture radar (InSAR) and pixel tracking techniques to image the coseismic deformation produced by the earthquake. The deformation measurement was used to determine the fault geometry and the coseismic distributed slip model with a constrained least square algorithm based on the homogeneous elastic half-space model. We divided the fault into four segments (named AS, BS, CS and DS, from the north to the south) in the inversion. The BS segment was almost parallel to the DS segment, the CS segment linked the BS and DS segments, and these three fault segments formed a fault step-over system. The Coulomb failure stress (CFS) change on the causative fault was also calculated. Results show that the maximum SAR line-of-sight (LOS) and horizontal deformation were −1.8 m and 3.6 m, respectively. The earthquake ruptured a 210-km-long fault with variable strike angles. The ruptured pattern of the causative fault is mainly a sinistral slip. Almost-pure normal characteristics could be identified along the fault segment across the Palu bay, which could be one of the factors resulting in the tsunami. The main slip area was concentrated at the depths of 0–20 km, and the maximum slip was 3.9 m. The estimated geodetic moment of the earthquake was 1.4×10^{20} Nm, equivalent to an earthquake of Mw 7.4. The CFS results demonstrate that the fault step-over of 5.3 km width did not terminate the rupture propagation of the main shock to the south. Two M>6 earthquakes (the 23 January 2005 and the 18 August 2012) decreased CFS along CS segment and the middle part of DS segment of the 2018 main shock. This implies that the stress release during the previous two earthquakes may have played a vital role in controlling the coseismic slip pattern of the 2018 earthquake.

Keywords: Palu earthquake; InSAR; coseismic slip model; source characteristics; step-over

1. Introduction

Eastern Indonesia, a region of a complex neotectonics [1], is located at the convergence zone of the Philippine Sea, and the Australian and Sunda tectonic plates [2,3] (Figure 1). The Australian and the Philippine Sea plates subduct beneath the Sunda plate at rates of 6 and 9 cm/yr, respectively [4]. Consequently, eastern Indonesia is highly seismically active; rapid rotations of local small tectonic blocks occur in this region [3]. The Palu-Koro Fault (Figure 1), the most prominent active fault of

Sulawesi straddled by Palu City, bisects Sulawesi Island, with the Sula block on the northeast and the South Sulawesi block on the southwest. The South Sulawesi block rotates anticlockwise at a rate of about 1°/Ma, while the Sula Block rotates clockwise at a rate of about 4°/Ma [4]. The relative motion between these two blocks is accommodated by the sinistral slip along the Palu-Koro Fault at a rate of 42 mm/yr [3]. Stevens et al. [5], from observing the fast slip rate measured by GPS and the historical seismicity data, deduced that the left-lateral Palu-Koro Fault stored enough strain to produce an earthquake bigger than Mw 7.

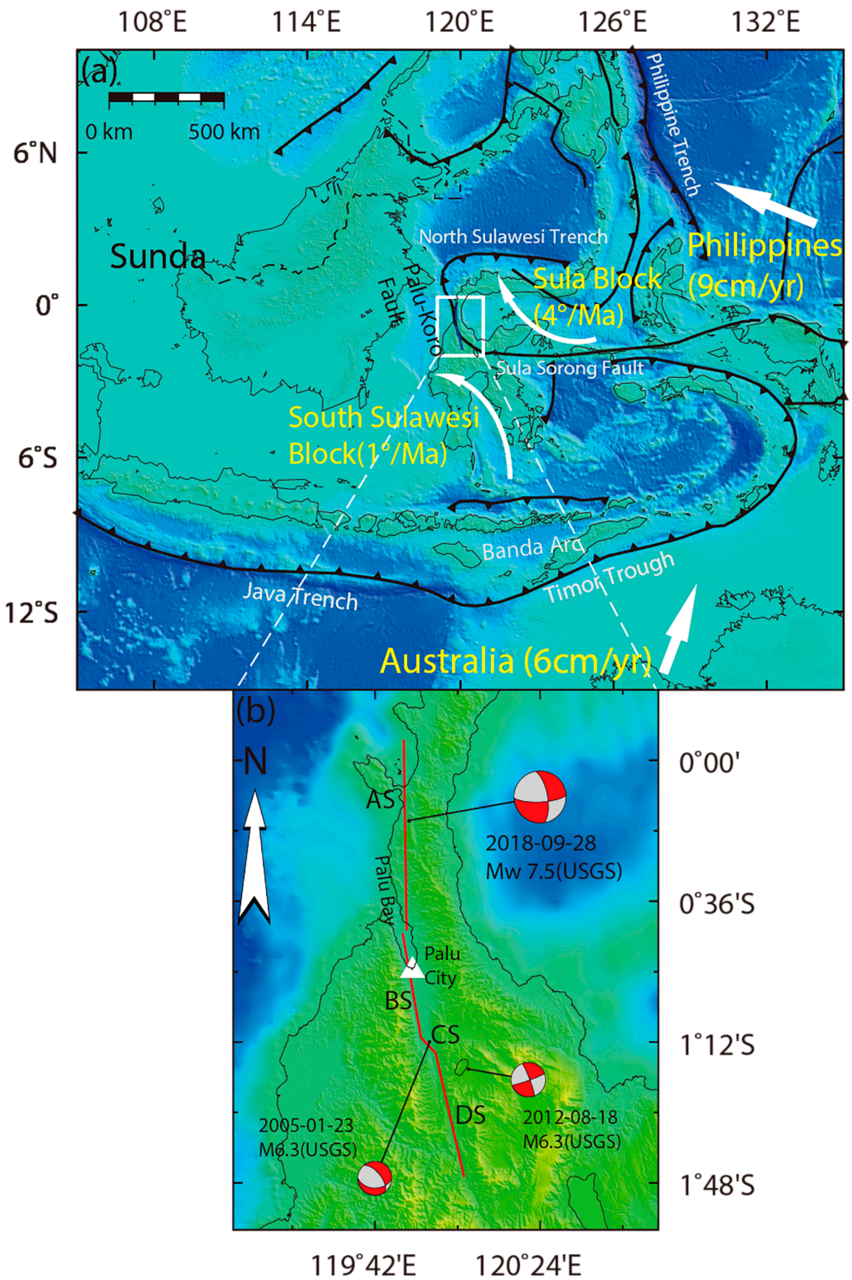

Figure 1. The seismotectonic setting of the Sulawesi Island and area studied in this paper. (**a**) White straight arrows show displacement directions of the Australia and Philippine Sea tectonic plates relative to the Sunda plate. White curved arrows show rotation directions of the South Sulawesi block and the Sula block. White rectangle corresponds to the study area (**b**). (**b**) Red lines delineate the seismogenic fault, which is divided into four segments named AS, BS, CS, and DS, from north to south. The largest red beach ball diagram indicates the epicenter and the focal mechanism of the main shock. The two smaller red beach ball diagrams are the nearest historical earthquakes of magnitude greater than 6.

On 28 September 2018, at 10:02:45 (UTC), an Mw 7.4 earthquake hit central Sulawesi, Indonesia. The epicenter (0.256°S, 119.846°E), determined by the United States Geological Survey (USGS), was located about 80 km north of Palu City (Figure 1). Both the USGS and the gCMT (global CMT: https//:www.globalcmt.org) provided the focal mechanism solutions, which indicated that the earthquake occurred on the north section of the Palu-Koro Fault, a predominantly sinistral fault with a normal component. The event resulted in catastrophic soil liquefaction; it heavily destroyed infrastructure and dwellings, and killed around 2101 people in the central Sulawesi region [6]. Another important factor that led to such a severe disaster was the tsunami that followed the main shock. The tsunami generated massive waves of 2–6 m in height and inundated the region along the coast of Palu Bay.

Synthetic aperture radar (SAR) images large areas with high spatial resolution in all weather conditions. Spaceborne or airborne SAR data are used for estimating the damage produced by natural and anthropogenic hazards [7–9]. The interferometric synthetic aperture radar (InSAR) technique, used for mapping very small surface motions [10], was successfully applied for the first time to detect coseismic deformation by Massonnet et al. [11]. Weston et al. [12] showed that the differences of seismic moments computed from InSAR and gCMT are relatively small. Presently, the InSAR technique plays a vital role and is widely used for the measurement of surface deformation produced by earthquakes [13–17].

It was known that the Palu-Koro Fault is capable of generating super-shear ruptures [1]. Socquet et al. [18] provided evidence, derived from optical and SAR data, that a segment of the Palu-Koro Fault was ruptured at super-shear velocities. Zhang et al. [19] estimated the rupture process of the main shock by jointly inverting the InSAR and seismic data. Bao et al. [20] demonstrated that the 2018 Palu earthquake ruptured at a sustained velocity of 4.1 km/s, and characterized an early and persistent super-shear rupture using tele-seismic and satellite image data. Super-shear rupture characteristics of this event was also proved by Fang et al. [21] by inverting InSAR and broadband regional seismogram data. Song et al. [22] also investigated the fault rupture and slip model of this earthquake with ALOS-2 InSAR data. However, the previous studies payed less attention to the complex fault structures and their implications on the rupture termination. No detailed study has been carried out yet on the impact of the historical regional earthquakes on the slip patterns of the 2018 event.

In this study, we firstly map the coseismic deformation field using two tracks of ALOS-2 SAR data with InSAR and pixel tracking techniques. The horizontal deformation map derived in this study is used to delineate the fault trace. Then, we use InSAR data to infer the distributed slip model of the earthquake and analyze the source characteristics of this event. Finally, we calculate the CFS change on each segments of the earthquake fault and discuss the potential effects of previous M ~6 earthquakes on rupture termination during the earthquake.

2. Materials and Methods

2.1. ALOS-2 SAR Data and Processing

Before and after the 2018 Palu earthquake, several SAR satellites collected measurements covering the Sulawesi Island. C-band (wavelength of 5.6 cm) Sentinel-1 SAR data were provided freely by the European Space Agency. These post-event data have been used for rapid building damage mapping for this event [23]. However, due to the short wavelength, the Sentinel-1 SAR coseismic interferograms show strong decorrelation in this area, so they were not used in this study. L-band (wavelength of 24 cm) ALOS-2 SAR data were provided by the Japan Aerospace Exploration Agency (JAXA) under research announcement (RA). In dense vegetation areas, L-band data maintains high coherence during InSAR processing. In this study, we used two descending ALOS-2 ScanSAR (wide swath) paths from JAXA spanning from 21 August 2018 to 11 October 2018 (Table 1) to image the coseismic deformation associated with this event.

Table 1. Details of ALOS-2 SAR data used in this study.

Path Number	Acquisition Time (M-D-Y)	Heading Angle (°)	Incidence Angle (°)
25	09-27-2018 10-11-2018	195	39
26	08-21-2018 10-02-2018	195	39

The ALOS-2 SAR data provided by JAXA were in the single look complex (SLC) format. We used the SARscape 5.4 software to generate coseismic interferograms. To obtain the along-track deformation, we used an automated processing system, gInSAR [15], which was originally developed to work with the GAMMA software [24] at the Canada Centre for Remote Science (CCRS) of the Natural Resources Canada. The multi-look of azimuth and range for both tracks are 15 and 2, respectively. The 90 m resolution shuttle radar topography mission (SRTM) v4.1 digital elevation model (DEM) data [25] were used to resample slave SAR image to master ones, remove the topographic phase in the interferograms and geocode the unwrapped interferograms into WGS-84 geographic coordinates. To better improve the quality of the interferograms before unwrapping, an adaptive Goldstein filter method [26] was used in the processing. The minimum cost flow algorithm [27,28] was applied to unwrap the interferograms. Orbital and ionospheric effects in the final interferograms were reduced by fitting and subtracting a polynomial model [29]. The coseismic interferogram of path 26 has similar viewing geometry as the path 25 interferogram (Figure 2b, Table 1) and does not cover the entire deformation area of the earthquake. Therefore, for the inversion we selected the path 26 along-track deformation (Figure 2a) and the path 25 line-of-sight (LOS) deformation (Figure 2c) converted from the unwrapped interferometric phase. Another two tracks of RADARSAT-2 data were also processed in this study. Due to strong decorrelation, only along-track measurements were selected to validate the final slip model, which were not used in the inversion.

Figure 2 shows that the area affected by this event is about 100 km in width and 200 km in length. The pixels with an interferometric coherence less than 0.3 were masked out due to limited reliability. The coseismic deformation fields show that the PALSAR-2 data maintain a reliable interferometric coherence in central Sulawesi. An obvious boundary line between positive and negative horizontal deformation values can be spotted in Figure 2a, implying that the earthquake broke the surface during the main shock [30]. On the right side of the fault trace, the northern displacement at the surface reached −3.6 m. The southern displacement on the left side reached 3.6 m. This deformation pattern directly implies that the left-lateral strike-slip mechanism of the earthquake occurred, which is identical to the focal mechanism derived from seismic data. It should be noted that the along-track deformation field does not cover the whole region of the main seismic zone. Figure 2b shows that the densest fringes are found in the region around Palu City, which is the reason why Palu City was significantly damaged by this event. The presence of another area of large deformation implies slip partitioning during the earthquake. The right area moves away from the satellite at a maximum of −1.8 m, and the left area moves toward the satellite at a maximum of 0.7 m.

Using the pixel tracking technique, we obtained the sub-pixel offsets along the satellite track by maximizing the cross-correlation coefficient [31]. Precision in this technique depends on the size of the SAR image pixel, which is generally low [32]. In this study, we only used the LOS coseismic deformation to constraint the slip model. The along-track deformation was only used to delineate the fault trace. The obtained LOS deformation is made up of tens of millions of pixel observations, and it is impossible to include all the samples in the inversion. We therefore down-sampled the original observations using a uniform sampling [33] to reduce the number of observations to 7709 (Figure S1).

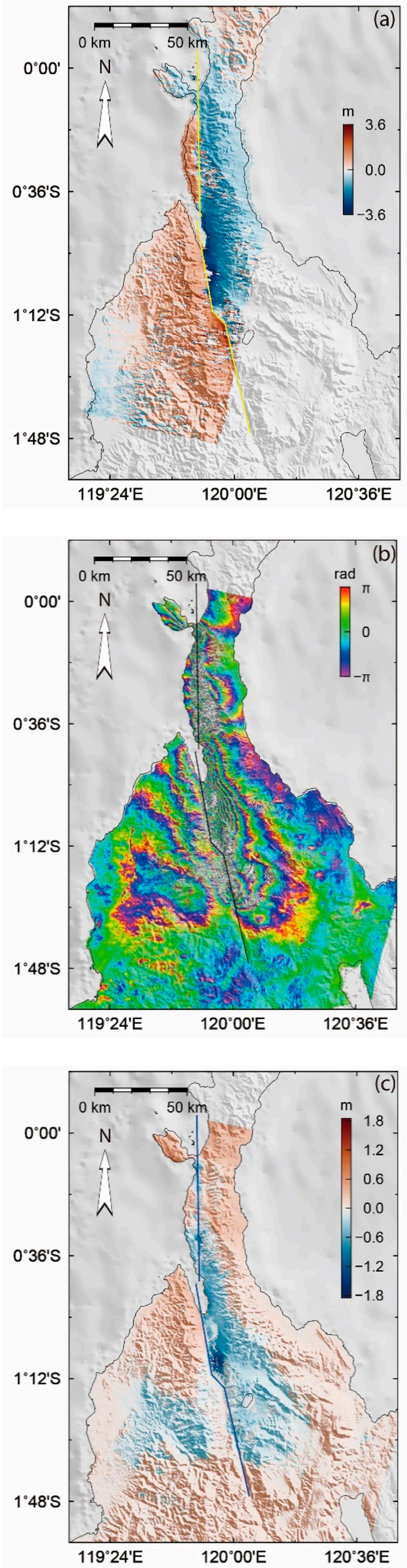

Figure 2. (**a**) Along-track displacement of path 26. Negative values represent northward motion. (**b**) Interferogram of path 25, each color cycle represents 15 cm of line-of-sight (LOS) displacement. (**c**) LOS displacement of path 25, which is converted from the unwrapped interferogram. Positive indicates that the surface is moving toward the satellite.

2.2. Modeling Method

The premise of inverting for the fault slip model is to determine the geometric parameters of the seismogenic fault. Based on the along-track deformation map, the earthquake broke surface and the location of the seismogenic fault can then be fixed in a similar way to Feng et al. [34]. It can be seen from the along-track deformation map that the trace of the surface rupture is a very irregular curve. For simplicity, we identified that the part on the Sulawesi Neck area is the first segment of the fault. The south part of the fault trace around Palu City shows a straight linear trend, therefore, this section was used as the second segment. At the south of the second segment, there is a nearly straight northwest-southeastern trace part. This would be the third segment of the seismogenic fault. At the southernmost end of the third segment, only a small portion of the trace can be seen. According to the geomorphological features shown in the SRTM DEM, we defined this segment as the fourth segment. For the sake of calculation, we extended these four segments appropriately. From north to south, the four segments were named AS, BS, CS and DS. Consequently, the geometric parameters (Table 2), including strike, length and geometric position, were determined based on the along-track deformation field. The focal mechanism of this event provided by USGS had a dipping angle of 67° to the east. Walpersdorf et al. [35], using GPS data, and Socquet et al. [3], using GPS and earthquake slip vector data, pointed out that the locking depth of the Palu-Koro Fault is 12 km. The locking depth between 2 and 8 km has also been inverted using GPS measurements by Stevens et al. [5]. Therefore, we fixed the width of the fault to 20 km and the dip angle to 67° in the inversion.

Table 2. Geometric parameters of the causative fault.

Segment Name	Top Center Lon	Top Center Lat	Strike	Dip	Length	Width
	°	°	°	°	km	Km
AS	119.8278	−0.3187	359.14	67	90	20
BS	119.8558	−0.9587	349.98	67	50	20
CS	119.9258	−1.2140	316.72	67	10	20
DS	120.0171	−1.5109	347.11	67	60	20

The USGS and gCMT focal mechanisms suggest an overall average mechanism of the entire rupture history of the earthquake. Zhang et al. [36] proposed a method to estimate source mechanism variations using geodetic data based on point dislocation sources with multiple uniform slip fault segments along the rupture, which is useful to better understand the variations of ruptures. Zhang et al. [19] also investigated the Palu earthquake with the six separate fault segments using this method. In order to achieve more details about the source mechanism variations, here, we divided the four segments into 21 sections, each with a length of 10 km. As the geometric parameters of each section have been fixed, the slip on each section is linear only to the surface displacements based on the homogeneous elastic half-space rectangular model [37]. Assuming that the northmost and the southmost sections did not slip, we used a constrained bounded linear least squares method to solve for the slip and the source mechanism variations.

To reveal more details of the source characteristics, we inverted the coseismic LOS deformation for the distributed slip of the 2018 Palu earthquake. The width of the fault was extended to 30 km, and a depth-based fault dividing method [38,39] was applied to split the individual fault segment into distributed sub-faults, in which the size of individual fault patches varied with depth, and a damping factor of 1.05 was adopted. We finally created 813 small fault patches to use in the inversion. We re-calculated the Green's matrix of the unit slip with the 813 faults based on Okada's analytical solution model [37]. We set up zero-slip on the fault patches along the fault boundaries in the inversion, while the fault patches on top were allowed to slip [40]. The slip on each fault patch then could be retrieved by reaching the minimum of an objective function [41,42] with the bounded constrained least squares method:

$$F(s) = \| G\, s - d \|^2 + \kappa^2 \| L\, s \|^2 \tag{1}$$

where G is the source dislocation Green's matrix, s is the distributed slip, d is the LOS surface displacement observations, and L is the finite difference approximation of the Laplacian operator. κ is the smoothing factor, which can be determined from the trade-off curve function between the misfit and the solution roughness. In this study, we selected the smoothing factor of 0.9 (Figure S2).

2.3. CFS Change Calculation

It is believed that coseismic CFS change can play an important role in investigating the interactions between fault segments [17,43,44] during earthquakes. Based on the previous seismic data solutions of the previous studies [19,20], the Palu earthquake ruptured unilaterally from north to south. Therefore, we calculated the CFS change on the four fault segments caused by the rupture of the four segments in turn from north to south, to quantitatively investigate their interaction during the rupture. The receiver and the source parameters of each fault segment, including the strike, dip and rake angle, were all from our inverted slip model.

When a slip happens on a source fault, the CFS can be added in the neighboring region permanently. The CFS change consists of the shear stress change (positive in the slip direction) and the normal stress change (positive when the fault is clamped). A CFS change can then be calculated as follows [45]:

$$\Delta CFS = \Delta\tau + \mu' \, \Delta\sigma_n \tag{2}$$

where $\Delta\tau$ is the shear stress change, $\Delta\sigma_n$ is the normal stress change and μ' is the effective coefficient of friction on the fault.

An increase in CFS (positive values) on the receiver fault promotes failure, and oppositely a decrease in CFS (negative values) retards failure. In this study, we applied the friction coefficient of 0.4 in the computation. We used the open source software Coulomb v3.4 [46] to calculate the CFS change on the four fault segments during the source rupture.

3. Results

3.1. Slip Model

The solved spatial source mechanism variations are presented in Figure 3. From north to south, there are thrust, right lateral slip, sinistral strike-slip, and normal motion-dominated mechanisms. Assuming the rigidity modulus is 30 Gpa, we observed a segment with the largest moment magnitude of 6.8, which is located at the northern second 10 km-long section (Figure 3). The smallest magnitude was 5.7, except for the northernmost and the southernmost section, located at the southern third 10 km-long section. It was noted that an almost pure normal slip could be observed along the segment around the Palu Bay. We reproduced the LOS observations (Figure S3) based on the multiple-segment uniform slip model of the earthquake. The root mean square (RMS) misfit of the model is 8.4 cm.

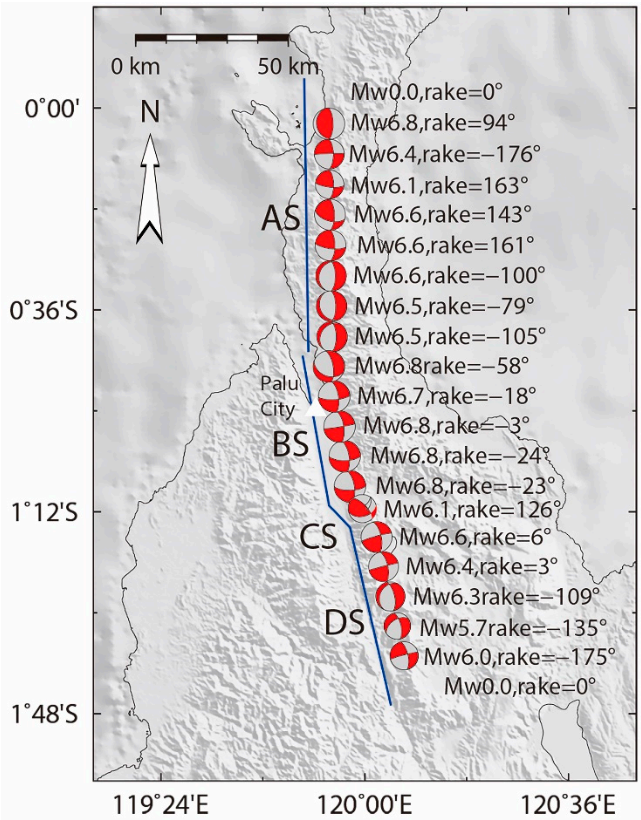

Figure 3. Spatial source mechanism variations. Red beach balls are drawn using the mechanisms of each section. The rake angle of each section is given on the right of each ball.

The preferred coseismic distributed slip determined from the InSAR displacements is shown in Figure 4, which reveals that the earthquake was dominated by sinistral motions with normal and thrust components in several individual segments. The maximum slip of ~4 m reached the surface along the segment of BS (Figure 4), and the major slip (>1 m) was concentrated in the fault zone shallower than 16 km in depth. With a shear modulus of 30 Gpa, the estimated geodetic moment is 1.4×10^{20} Nm, equivalent to an earthquake of Mw 7.4, which is smaller than previous studies [21,22]. We calculated the synthetic LOS displacements (Figure 5a) based on the preferred fault slip model, and the residual between the synthetic and observed displacement is shown in Figure 5b. The RMS misfit decreased to 6.6 cm based on the distributed slip.

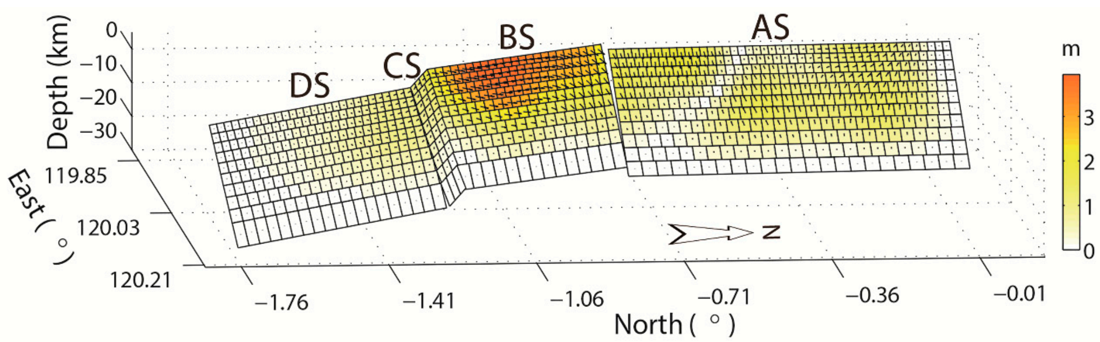

Figure 4. Coseismic slip distribution. Arrows represent the slip directions on each patch.

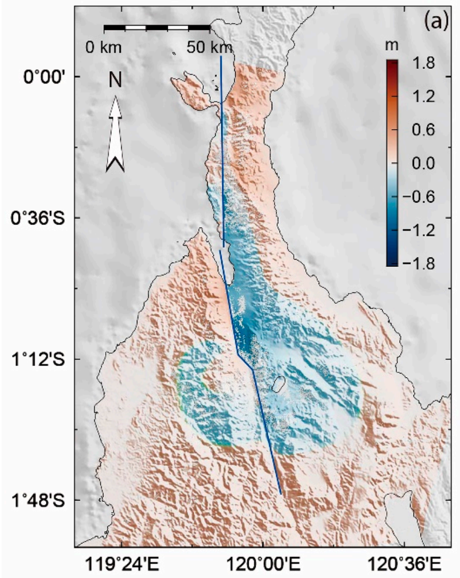

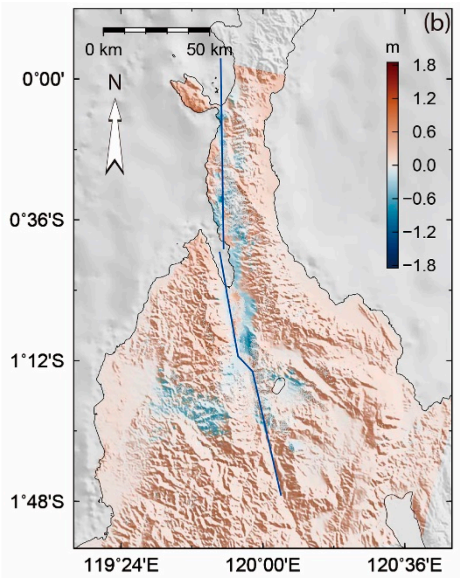

Figure 5. (**a**) The synthetic line-of-sight (LOS) displacement based on the preferred distributed slip model. (**b**) The residual between the observed and the synthetic LOS displacements.

3.2. CFS Change

To test the effects of the CFS changes between different fault segments, we calculated accumulated CFS changes on the individual fault segments based on the slip model (Figure 4). As the earthquake ruptured unilaterally with an initiation on the north, based on the previous studies [19,20], it is reasonable to examine the permanent stress change processes on the earthquake fault from the slip of the early rupture from north to south. As shown in Figure 6, the CFS increased mainly on the BS due to the rupture of AS with up to 10 bar, and the CFS changes on the fault segments of CS and DS were negligible (Figure 6a). At the next stage, the rupture of AS and BS resulted in a dramatic increase in CFS on the CS fault segment, and an increase on the DS fault segment as well (Figure 6b). The ruptures on the CS and DS fault segments can also mainly add stress perturbations on the later segments and do not change the stress patterns in the previous segments (Figure 6c,d). Note that the shortest segment, CS, always stayed in a loading status during the earthquake although it hosted limited slip (Figure 4).

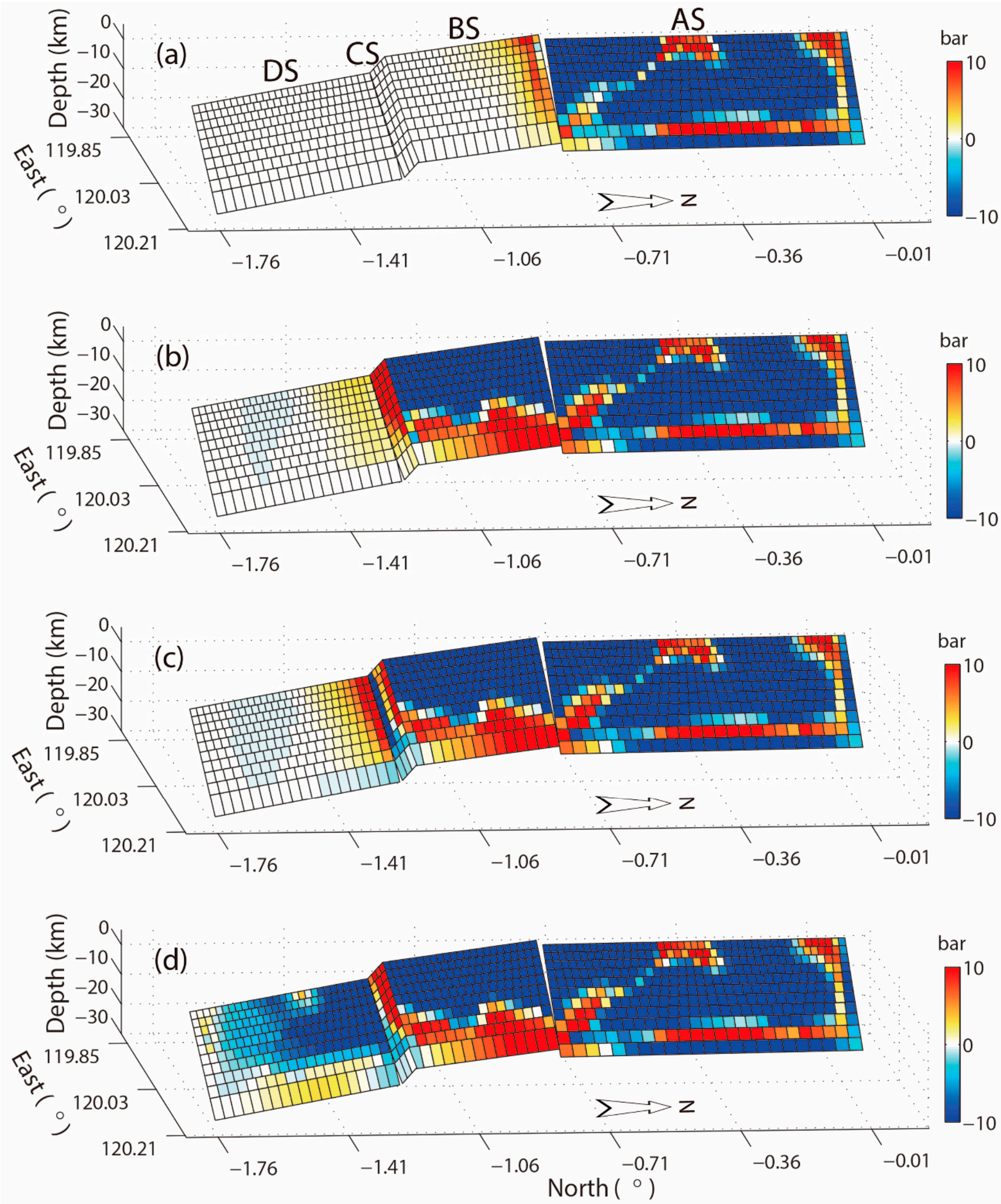

Figure 6. The CFS change on the fault plane. (**a**) Caused by AS rupture. (**b**) Caused by AS and BS rupture. (**c**) Caused by AS, BS and CS rupture. (**d**) Caused by rupture of all four fault segments.

4. Discussion

Our distributed slip model derived by inverting the ALOS-2 SAR data is basically consistent with the results of Fang et al. [21], Ulrich et al. [47] and Song et al. [22], including the moment magnitude and focal mechanism. The slip model shows that the 2018 Palu earthquake occurred on the Palu-Koro Fault, a sinistral strike-slip. The main slip was concentrated at depths of 0–20 km. Wanlpersdorf et al. [35] used GPS measurements to show that the Palu-Koro Fault was previously locked, and the locking depth was around 8–16 km based on a simple model. Stevens et al. [5] pointed out that the locking depth of the Palu Fault ranges between 2–8 km. Jiang et al. [48,49] believed that the coseismic slip depth is likely to be greater than the locking depth. In our study, the coseismic slip area was a little deeper than the locking depth. This demonstrates that our slip model is very consistent with the fault locking research. The main slip was concentrated in the area around Palu City, corresponding to the epicenter area issued by USGS and the central area of the AS. The main slip area is also identical to the I, II, III asperities pointed out by Fang et al. [21]. However, we cannot find a large slip on the DS, based on our slip model. A main normal slip area is observed in Palu Bay, while a thrust slip area is located to the north of Palu Bay. The characteristics of these two slip areas were also observed in the results of Ulrich et al. [47] and Fang et al. [21]. Song et al. [22] showed different slip patterns in their slip model, which may be because they introduced a submarine normal fault.

This event was followed by a deadly tsunami. Several researchers discussed the control factors of this deadly tsunami. Sassa et al. [50] thought gravity flow of the significant liquefaction could cause the tsunami. Heidarzadeh et al. [51] simulated the tsunami, and showed that the maximum coastal amplitude was far less than the observed tsunami wave height. The authors also deduced that the cause could be the submarine landslides. Omira et al. [52] carried out the post-tsunami survey, and suggested that the earthquake did not contribute. Zhang et al. [19] and Barnhart et al. [53] both suggested that landslides could have played a vital role in triggering the tsunami. So far, the real mechanism of this tsunami is not fully understood yet. It is widely accepted that a vertical block movement can create tsunami waves [54]. Kreemer et al. [55] thought that vertical deformation is critical in producing a tsunami. Geist et al. [56] indicated that if earthquakes greater than M 6.5–7 occurring beneath an ocean produce predominantly vertical deformation, they can generally generate tsunamis. From our source mechanism variation and the slip model, we found that the magnitude of the section in Palu Bay is 6.8, and that normal components are dominant on the northernmost BS and southernmost AS, which could have produced enough surface vertical deformation in the sea floor to cause the tsunami. We simulated the vertical displacement (Figure 7) in the Central Sulawesi area. From Figure 7, the submarine near the Pantoloan slumping is about 0.7 m. The de-tide sea level records show that tsunami records were caught for the Pantoloan [51]. Previous studies [47] believed that the vertical deformation in the Palu Bay generated by the main shock could be the primary tsunami source by modelling the tsunami amplitudes. Our slip model can produce significant vertical deformation on the sea floor and therefore, it may not be necessary to have an additional normal slip fault in the sea floor to explain the observed tsunami in this case. Note that tsunami simulation requires a certain specialty, which has been out of the scope of this study.

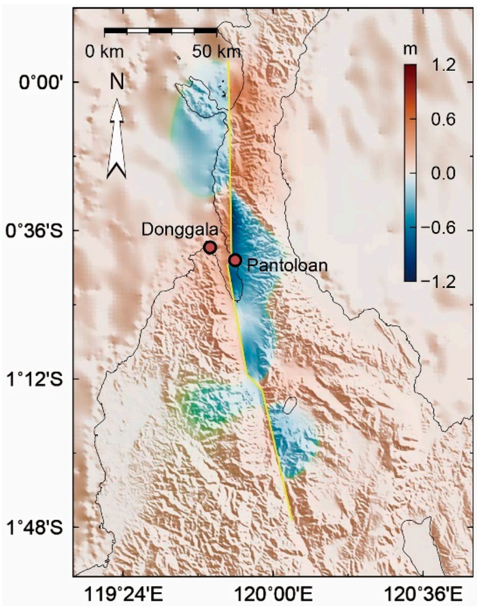

Figure 7. The simulated vertical displacement.

The Palu-Koro Fault was thought to be capable of generating super-shear ruptures and possessing the greatest seismic risk in Central Sulawesi [1]. The 2018 Palu earthquake occurred along the Palu-Koro Fault and has been quantitatively shown to be a super-shear rupture event [18]. However, what stopped the earthquake rupture is still unsolved. In this study, we calculated the CFS changes on the fault to analyze the termination of the rupture. We found that the geometrical relationship between the three south fault segments is very fascinating. The BS is almost parallel to the DS, with a distance between them of 5.3 km, and the CS links the BS and DS, with an intersection angle of 32°. This type of fault system is called a fault step-over. It is important to evaluate whether the fault step-over is capable of arresting and promoting the fault rupture. Bie et al. [57] pointed out that the fault steps may limit the earthquake size for strike-slip faults. Harris [58] studied the parallel strike-slip faults interaction, and the effect of fault step-over on fault ruptures. The results indicate that a fault step-over wider than 5 km often impedes the rupture of a sinistral earthquake. For a strike-slip fault system without a linking structure, a 5 km width of fault step-over is also a limit for rupture propagation [59]. It seems that the 5 km width of a fault step is the limit for strike-slip fault rupture. However, through a statistical analysis to examine the effects of fault step-overs on the rupture termination of 29 historical sinistral slip earthquakes in the world, Li et al. [60] found that the smallest fault step-over widths are different for different magnitude earthquakes. The step-over width in this event is very close to the width limit. Calculation of the CFS change is an effective tool to study the effect of fault step-over in the rupture propagation. Hodge [43] used coseismic CFS change to analyze the fault step-over effects in a normal fault system. King et al. [45] showed that a 4 bars CFS increase on fault will hasten great earthquake one decade. Due to the unilateral rupture pattern of the 2018 Palu earthquake, it is very suitable for analyzing the step-over effect in the fault rupture by calculating the CFS changes on the four fault segments. From the results of the CFS change calculation, we found that the ruptures of AS and BS make the CFS on CS dramatically increase, with a smaller increase on the DS. As the AS, BS and CS ruptured, the CFS on the DS continued to increase. Therefore, we cannot draw the conclusion that a step-over of 5.3 m width retarded or terminated the rupture of the fault.

Wei et al. [61] speculated that the rupture stopped due to a stress shadow caused by two historical earthquakes, which are around 40 km away from the 2018 event. They proposed that the occurrence of the historical earthquakes could have created a stress shadow in the epicentral area of the 2018 event, which could have played a role in stopping the 2018 Palu earthquake. Following this idea, we referred to the earthquake catalog of USGS, and found that two previous earthquakes of magnitude greater than 6. The earthquakes of 23 January 2005 and 18 August 2012 occurred near the Palu area (Figure 1b). We calculated the permanent CFS changes on the four fault segments induced by the two earthquakes. We constructed the model parameters (Table S1) of the two earthquakes based on the moment tensor mechanisms of USGS. The receiver fault parameters are also from our preferred slip model. The result (Figure 8) shows that the ruptures of the two M 6.3 earthquakes resulted in a CFS decrease on both the CS and the middle part of DS, and a CFS increase on the north part of DS. The decreases in the CFS on the middle DS and CS segments are intriguingly consistent with the 2018 Palu earthquake faults hosting limited slip, particularly on the step-over of CS.

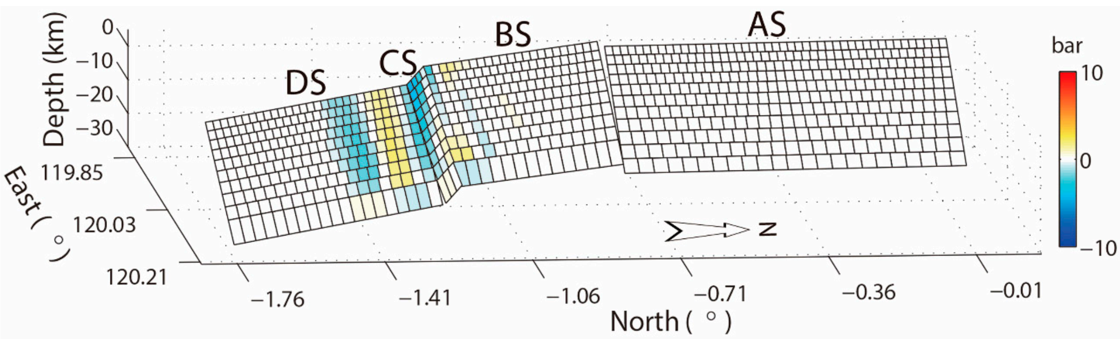

Figure 8. The CFS changes on the AS, BS, CS and DS affected by the 2005 M 6.3 earthquake and the 2012 M 6.3 earthquake.

5. Conclusions

We obtained along-track and LOS InSAR coseismic deformation fields for the 2018 Palu earthquake using ALOS-2 SAR data. Source mechanism variations and a preferred slip model were derived from the coseismic deformation, indicating that the rupture of 2018 Palu earthquake is of mainly sinistral slip and presents normal characteristics across the Palu bay. With a shear modulus of 30 Gpa, the estimated geodetic moment is 1.4×10^{20} Nm, equivalent to an earthquake of Mw 7.4. The calculated CFS change results show that the 5.3 km-width step-over did not retard the rupture to the south. However, the Coulomb stress drop produced by the two previous earthquakes of the 23 January 2005 and the 18 August 2012 in the Palu area, may have arrested the continuous rupture of this event to the south.

Supplementary Materials: The following are available online at http://www.mdpi.com/2072-4292/11/17/1999/s1, Figure S1: Downsampled line-of sight (LOS) deformation observations, Figure S2: Trade-off curve between misfit and solution roughness, Figure S3: Synthetic LOS deformation based on the source mechanism variation model and residual LOS deformation between the observed and synthetic deformation, Table S1: The source parameters of the 2005 M 6.3 and the 2012 M 6.3 earthquakes constructed.

Author Contributions: Conceptualization, Y.W.; Formal analysis, Y.W.; Investigation, Y.W., W.F. and K.C.; Methodology, Y.W. and W.F.; Resources, Y.W., W.F. and S.S.; Supervision, Y.W.; Visualization, Y.W.; Writing—original draft, Y.W.; Writing—review & editing, Y.W., W.F., K.C. and S.S.

Funding: This research was funded by the National Key R&D Program of China, grant number 2018YFC1504501.

Acknowledgments: The ALOS-2 SAR data were provided by JAXA through the ALOS-2 RA6 Projects (PI Numbers: 3125 and 3159). The Harris Geospatial Solutions Team sent the trial runtime license to process the ALOS-2 SAR data using SARscape 5.4. We also thank Leyang Wang at the East China University of Technology, Hua Gao at the Wuhan University and Xu Zhang at the Institute of Geophysics, China Earthquake Administration for discussing plotting the slip distribution. Figures were plotted using Generic Mapping Tools (GMT) [62].

Conflicts of Interest: The authors declare no conflict of interest.

References

1. Watkinson, I.M.; Hall, R. Fault systems of the eastern Indonesian triple junction: Evaluation of Quaternary activity and implications for seismic hazards. *Geol. Soc. Lond. Spec. Publ.* **2016**, *441*, SP441.448. [CrossRef]
2. Bellier, O.; Sébrier, M.; Beaudouin, T.; Villeneuve, M.; Braucher, R.; Bourles, D.; Siame, L.; Putranto, E.; Pratomo, I.J.T.N. High slip rate for a low seismicity along the Palu-Koro active fault in central Sulawesi (Indonesia). *Terra Nova* **2001**, *13*, 463–470. [CrossRef]
3. Socquet, A.; Simons, W.; Vigny, C.; McCaffrey, R.; Subarya, C.; Sarsito, D.; Ambrosius, B.; Spakman, W. Microblock rotations and fault coupling in SE Asia triple junction (Sulawesi, Indonesia) from GPS and earthquake slip vector data. *J. Geophys. Res. Solid Earth* **2006**, *111*, 1–15. [CrossRef]
4. Vigny, C.; Perfettini, H.; Walpersdorf, A.; Lemoine, A.; Simons, W.; Van Loon, D.; Ambrosius, B.; Stevens, C.; McCaffrey, R.; Morgan, P.; et al. Migration of seismicity and earthquake interactions monitored by GPS in SE Asia triple junction: Sulawesi, Indonesia. *J. Geophys. Res. Solid Earth* **2002**, *107*, ETG 7-1–ETG 7-11. [CrossRef]
5. Stevens, C.; McCaffrey, R.; Bock, Y.; Genrich, J.; Subarya, C.; Puntodewo, S.S.O.; Vigny, C. Rapid rotations about a vertical axis in a collisional setting revealed by the Palu fault, Sulawesi, Indonesia. *Geophys. Res. Lett.* **1999**, *26*, 2677–2680. [CrossRef]
6. Syifa, M.; Kadavi, P.R.; Lee, C.W. An Artificial Intelligence Application for Post-Earthquake Damage Mapping in Palu, Central Sulawesi, Indonesia. *Sensors* **2019**, *19*, 542. [CrossRef]
7. Liao, J. Detection of land surface change due to the Wenchuan earthquake using multitemporal advanced land observation satellite-phased array type L-band synthetic aperture radar data. *J. Appl. Remote Sens.* **2009**, *3*, 031680. [CrossRef]
8. Satake, M.; Kobayashi, T.; Uemoto, J.; Umehara, T.; Kojima, S.; Matsuoka, T.; Nadai, A.; Uratsuka, S. Damage estimation of the Great East Japan earthquake with airborne SAR (PI-SAR2) data. In Proceedings of the 2012 IEEE International Geoscience and Remote Sensing Symposium, Munich, Germany, 22–27 July 2012; pp. 1190–1191.

9. Uemoto, J.; Moriyama, T.; Nadai, A.; Kojima, S.; Umehara, T. Landslide detection based on height and amplitude differences using pre-and post-event airborne X-band SAR data. *Nat. Hazards* **2019**, *95*, 485–503. [CrossRef]
10. Gabriel, A.K.; Goldstein, R.M.; Zebker, H.A. Mapping small elevation changes over large areas: Differential radar interferometry. *J. Geophys. Res. Solid Earth* **1989**, *94*, 9183–9191. [CrossRef]
11. Massonnet, D.; Rossi, M.; Carmona, C.; Adragna, F.; Pelter, G.; Feigl, K.; Rabaute, T. The displacement field of the Landers earthquake mapped by radar interferometry. *Nature* **1993**, *364*, 138–142. [CrossRef]
12. Weston, J.; Ferreira, A.M.G.; Funning, G.J. Global compilation of interferometric synthetic aperture radar earthquake source models: 1. Comparisons with seismic catalogs. *J. Geophys. Res.* **2011**, *116*. [CrossRef]
13. Lasserre, C.; Peltzer, G.; Crampre, F.; Klinger, Y.; Woerd, J.V.d.; Tapponnier, P. Coseismic deformation of the 2001 Mw=7.8 Kokoxili earthquake in Tibet, measured by synthetic aperture radar interferometry. *J. Geophys. Res.* **2005**, *110*, B12408. [CrossRef]
14. Wang, Y.; Zhu, J.; Ou, Z.; Li, Z.; Xing, X. Coseismic slip distribution of 2009 L'Aquila earthquake derived from InSAR and GPS data. *J. Cent. South Univ.* **2012**, *19*, 244–251. [CrossRef]
15. Feng, W.; Tian, Y.; Zhang, Y.; Samsonov, S.; Almeida, R.; Liu, P. A Slip Gap of the 2016Mw 6.6 Muji, Xinjiang, China, Earthquake Inferred from Sentinel-1 TOPS Interferometry. *Seismol. Res. Lett.* **2017**, *88*, 1054–1064. [CrossRef]
16. Funning, G.J.; Parsons, B.; Wrigth, T.J.; Jackson, J.A.; Fielding, E. Surface displacements and source paramenters of the 2003 Bam (Iran) earthquake from Envisat advanced synthetic aperture radar imagery. *J. Geophys. Res.* **2005**, *110*. [CrossRef]
17. Xu, W.; Feng, G.; Meng, L.; Zhang, A.; Ampuero, J.P.; Bürgmann, R.; Fang, L. Transpressional Rupture Cascade of the 2016 Mw 7.8 Kaikoura Earthquake, New Zealand. *J. Geophys. Res. Solid Earth* **2018**, *123*, 2396–2409. [CrossRef]
18. Socquet, A.; Hollingsworth, J.; Pathier, E.; Bouchon, M. Evidence of supershear during the 2018 magnitude 7.5 Palu earthquake from space geodesy. *Nat. Geosci.* **2019**, *12*, 192–199. [CrossRef]
19. Zhang, Y.; Chen, Y.; Feng, W. Complex multiple-segment ruptures of the 28 September 2018, Sulawesi, Indonesia, earthquake. *Sci. Bull.* **2019**, *64*, 650–652. [CrossRef]
20. Bao, H.; Ampuero, J.-P.; Meng, L.; Fielding, E.J.; Liang, C.; Milliner, C.W.D.; Feng, T.; Huang, H. Early and persistent supershear rupture of the 2018 magnitude 7.5 Palu earthquake. *Nat. Geosci.* **2019**, *12*, 200–205. [CrossRef]
21. Fang, J.; Xu, C.; Wen, Y.; Wang, S.; Xu, G.; Zhao, Y.; Yi, L. The 2018 Mw 7.5 Palu Earthquake: A Supershear Rupture Event Constrained by InSAR and Broadband Regional Seismograms. *Remote Sens.* **2019**, *11*, 1330. [CrossRef]
22. Song, X.; Zhang, Y.; Shan, X.; Liu, Y.; Gong, W.; Qu, C. Geodetic Observations of the 2018 Mw 7.5 Sulawesi Earthquake and Its Implications for the Kinematics of the Palu Fault. *Geophys. Res. Lett.* **2019**, *46*, 4212–4220. [CrossRef]
23. Adriano, B.; Xia, J.; Baier, G.; Yokoya, N.; Koshimura, S. Multi-Source Data Fusion Based on Ensemble Learning for Rapid Building Damage Mapping during the 2018 Sulawesi Earthquake and Tsunami in Palu, Indonesia. *Remote Sens.* **2019**, *11*, 886. [CrossRef]
24. Wegmüller, U.; Werner, C. Gamma SAR processor and interferometry software. In Proceedings of the Third ERS Symposium on Space at the service of our Environment, Florence, Italy, 14–21 March 1997; pp. 1686–1692.
25. Farr, T.G.; Rosen, P.A.; Caro, E.; Crippen, R.; Duren, R.; Hensley, S.; Kobrick, M.; Paller, M.; Rodriguez, E.; Roth, L. The shuttle radar topography mission. *Rev. Geophys.* **2007**, *45*. [CrossRef]
26. Goldstein, R.M.; Werner, C.L. Radar interferogram filtering for geophysical applications. *Geophys. Res. Lett.* **1998**, *25*, 4035–4038. [CrossRef]
27. Costantini, M. A novel phase unwrapping method based on network programming. *IEEE Trans. Geosci. Remote Sens.* **1998**, *36*, 813–821. [CrossRef]
28. Chen, C.W.; Zebker, H.A. Network approaches to two-dimensional phase unwrapping: Intractability and two new algorithms. *J. Opt. Soc. Am. A* **2000**, *17*, 401–414. [CrossRef]
29. Xu, B.; Li, Z.; Wang, Q.; Jiang, M.; Zhu, J.; Ding, X. A Refined Strategy for Removing Composite Errors of SAR Interferogram. *IEEE Geosci. Remote Sens. Lett.* **2014**, *11*, 143–147. [CrossRef]

30. Jónsson, S.; Zebker, H.; Segall, P.; Amelung, F. Fault Slip Distribution of the 1999 Mw7.1 Hector Mine, California Earthquake, Estimated from Satellite Radar and GPS Measurements. *Bull. Seism. Soc. Am.* **2002**, *92*, 1377–1389. [CrossRef]
31. Ou, D.; Tan, K.; Du, Q.; Chen, Y.; Ding, J. Decision Fusion of D-InSAR and Pixel Offset Tracking for Coal Mining Deformation Monitoring. *Remote Sens.* **2018**, *10*, 1055. [CrossRef]
32. Hu, J.; Li, Z.; Zhang, L.; Ding, X.; Zhu, J.; Sun, Q.; Ding, W. Correcting ionospheric effects and monitoring two-dimensional displacement fields with multiple-aperture InSAR technology with application to the Yushu earthquake. *Sci. China Earth Sci.* **2012**, *55*, 1961–1971. [CrossRef]
33. Wang, Y.; Zhu, J.; Li, Z.; Ou, Z. Coseismic slip distribution inversion of the 2011 Yushu earthquake using PALSAR data. *Acta Geod. Cartogr. Sin.* **2013**, *42*, 27–33.
34. Feng, G.; Hetland, E.A.; Ding, X.; Li, Z.; Zhang, L. Coseismic fault slip of the 2008 Mw 7.9 Wenchuan earthquake estimated from InSAR and GPS measurements. *Geophys. Res. Lett.* **2010**, *37*. [CrossRef]
35. Walpersdorf, A.; Vigny, C.; Subarya, C.; Manurung, P. Monitoring of the Palu-Koro Fault (Sulawesi) by GPS. *Geophys. Res. Lett.* **1998**, *25*, 2313–2316. [CrossRef]
36. Zhang, Y.; Wang, R. Geodetic inversion for source mechanism variations with application to the 2008 Mw7. 9 Wenchuan earthquake. *Geophys. J. Int.* **2015**, *200*, 1627–1635. [CrossRef]
37. Okada, Y. Surface Deformation Due to Shear and tensile faults in a half-space. *Bull. Seism. Soc. Am.* **1985**, *75*, 1135–1154.
38. Fialko, Y. Probing the mechanical properties of seismically active crust with space geodesy: Study of the co-seismic deformation due to the 1992 Mw7.3 Landers (southern California) earthquake. *J. Geophys. Res.* **2004**, *109*. [CrossRef]
39. Xu, X.; Tong, X.; Sandwell, D.T.; Milliner, C.W.D.; Dolan, J.F.; Hollingsworth, J.; Leprince, S.; Ayoub, F. Refining the shallow slip deficit. *Geophys. J. Int.* **2016**, *204*, 1843–1862. [CrossRef]
40. Wang, K.; Fialko, Y. Space geodetic observations and models of postseismic deformation due to the 2005 M7.6 Kashmir (Pakistan) earthquake. *J. Geophys. Res. Solid Earth* **2014**. [CrossRef]
41. Wen, Y.; Xu, C.; Liu, Y.; Jiang, G. Deformation and Source Parameters of the 2015 Mw 6.5 Earthquake in Pishan, Western China, from Sentinel-1A and ALOS-2 Data. *Remote Sens.* **2016**, *8*, 134. [CrossRef]
42. Vajedian, S.; Motagh, M.; Mousavi, Z.; Motaghi, K.; Fielding, E.; Akbari, B.; Wetzel, H.-U.; Darabi, A. Coseismic Deformation Field of the Mw 7.3 12 November 2017 Sarpol-e Zahab (Iran) Earthquake: A Decoupling Horizon in the Northern Zagros Mountains Inferred from InSAR Observations. *Remote Sens.* **2018**, *10*, 1589. [CrossRef]
43. Hodge, M.; Fagereng, Å.; Biggs, J. The Role of Coseismic Coulomb Stress Changes in Shaping the Hard Link Between Normal Fault Segments. *J. Geophys. Res. Solid Earth* **2018**, *123*, 797–814. [CrossRef]
44. Yang, Y.-H.; Hu, J.-C.; Tung, H.; Tsai, M.-C.; Chen, Q.; Xu, Q.; Zhang, Y.-J.; Zhao, J.-J.; Liu, G.-X.; Xiong, J.-N.; et al. Co-Seismic and Postseismic Fault Models of the 2018 Mw 6.4 Hualien Earthquake Occurred in the Junction of Collision and Subduction Boundaries Offshore Eastern Taiwan. *Remote Sens.* **2018**, *10*, 1372. [CrossRef]
45. King, G.C.P.; Stein, R.S.; Lin, J. Static Stress Changes and the Triggering of Earthquakes. *Bull. Seism. Soc. Am.* **1994**, *84*, 935–953.
46. Toda, S. Forecasting the evolution of seismicity in southern California: Animations built on earthquake stress transfer. *J. Geophys. Res.* **2005**, *110*. [CrossRef]
47. Ulrich, T.; Vater, S.; Madden, E.H.; Behrens, J.; van Dinther, Y.; van Zelst, I.; Fielding, E.J.; Liang, C.; Gabriel, A.-A. Coupled, Physics-based Modeling Reveals Earthquake Displacements are Critical to the 2018 Palu, Sulawesi Tsunami. *Pure Appl. Geophys.* **2019**, 1–41. [CrossRef]
48. Jiang, J.; Lapusta, N. Connecting depth limits of interseismic locking, microseismicity, and large earthquakes in models of long-term fault slip. *J. Geophys. Res.: Solid Earth* **2017**, *122*, 6491–6523. [CrossRef]
49. Jiang, J.; Lapusta, N. Deeper penetration of large earthquakes on seismically quiescent faults. *Science* **2016**, *352*, 1293–1297. [CrossRef]
50. Sassa, S.; Takagawa, T. Liquefied gravity flow-induced tsunami: First evidence and comparison from the 2018 Indonesia Sulawesi earthquake and tsunami disasters. *Landslides* **2018**, *16*, 195–200. [CrossRef]
51. Heidarzadeh, M.; Muhari, A.; Wijanarto, A.B. Insights on the Source of the 28 September 2018 Sulawesi Tsunami, Indonesia Based on Spectral Analyses and Numerical Simulations. *Pure Appl. Geophys.* **2018**, *176*, 25–43. [CrossRef]

52. Omira, R.; Dogan, G.G.; Hidayat, R.; Husrin, S.; Prasetya, G.; Annunziato, A.; Proietti, C.; Probst, P.; Paparo, M.A.; Wronna, M.; et al. The September 28th, 2018, Tsunami in Palu-Sulawesi, Indonesia: A Post-Event Field Survey. *Pure Appl. Geophys.* **2019**, *176*, 1379–1395. [CrossRef]
53. Barnhart, W.D.; Hayes, G.P.; Wald, D.J. Global Earthquake Response with Imaging Geodesy: Recent Examples from the USGS NEIC. *Remote Sens.* **2019**, *11*, 1357. [CrossRef]
54. Hunt, B. A mechanism for tsunami generation. *J. Hydraul. Res.* **2010**, *31*, 111–120. [CrossRef]
55. Kreemer, C.; Holt, W.E.; Goes, S.; Govers, R. Active deformation in eastern Indonesia and the Philippines from GPS and seismicity data. *J. Geophys Res. Solid Earth* **2000**, *105*, 663–680. [CrossRef]
56. Geist, E.L.; Oglesby, D.D. Earthquake Mechanism and Seafloor Deformation for Tsunami Generation. In *Encyclopedia of Earthquake Engineering*; Beer, M., Kougioumtzoglou, I.A., Patelli, E., Au, I.S.-K., Eds.; Springer Berlin Heidelberg: Berlin, Germany, 2014; pp. 1–17. [CrossRef]
57. Bie, L.; González, P.J.; Rietbrock, A. Slip distribution of the 2015 Lefkada earthquake and its implications for fault segmentation. *Geophys. J. Int.* **2017**, *210*, 420–427. [CrossRef]
58. Harris, R.A.; Day, S.M. Dynamics of fault interaction: Parallel strike-slip faults. *J.Geophys. Res. Solid Earth* **1993**, *98*, 4461–4472. [CrossRef]
59. Harris, R.A.; Day, S.M. Dynamic 3D simulations of earthquakes on En Echelon Faults. *Geophys. Res. Lett.* **1999**, *26*, 2089–2092. [CrossRef]
60. Li, Z.; Zhou, B. Influence of fault steps on rupture termination of strike-slip earthquake faults. *J. Seismol.* **2017**, *22*, 487–498. [CrossRef]
61. Wei, S.; Feng, G.; Zeng, H.; Martin, S.; Shi, Q.; Muzli, M.; Wang, T.; Lindsey, E.; Triyono, R.; Hubbard, J.; et al. *The 2018 Mw 7.5 Palu Earthquake, a Gradually Accelerating Super-Shear Rupture Stopped by Stress Shadows in a Complex Fault System*; AGU Fall Meeting Abstracts: Washington, DC, USA, 2018.
62. Wessel, P.; Smith, W.H.F. New, improved version of generic mapping tools released. *EOS Trans. AGU* **1998**, *79*, 579. [CrossRef]